Science Advances
AAAS

advances.sciencemag.org/cgi/content/full/5/4/eaav3780/DC1

Supplementary Materials for

Origin of giant negative piezoelectricity in a layered van der Waals ferroelectric

Lu You, Yang Zhang, Shuang Zhou, Apoorva Chaturvedi, Samuel A. Morris, Fucai Liu, Lei Chang, Daichi Ichinose, Hiroshi Funakubo, Weijin Hu, Tom Wu, Zheng Liu, Shuai Dong*, Junling Wang*

*Corresponding author. Email: jlwang@ntu.edu.sg (J.W.); sdong@seu.edu.cn (S.D.)

Published 19 April 2019, *Sci. Adv.* **5**, eaav3780 (2019)
DOI: 10.1126/sciadv.aav3780

The PDF file includes:

Other Supplementary Material for this manuscript includes the following:

(available at advances.sciencemag.org/cgi/content/full/5/4/eaav3780/DC1)

Data file S1 (.cif format). Crystallographic information file (CIF) of unpoled CIPS crystal.
Data file S2 (.cif format). Crystallographic information file (CIF) of poled CIPS crystal.

Section S1. Full data series of the P-E and S-E measurements

Figures S1 and S2 show the voltage- and frequency-dependent P – E and S – E loops obtained from the static piezoelectric measurements. The results demonstrate good correlations between polarization and strain hysteresis curves, confirming the reliability of the methodology used. Note that the P – E loop of CIPS at 10 Hz (fig. S2B) becomes blown-up due to the contribution from its high ionic conductivity at room temperature (*57*). To reveal accurate polarization, the P – E loop of CIPS shown in the main text was obtained by subtracting the charge contribution from a linear resistor.

Section S2. Dynamic piezoelectric measurements

Figure S3 shows the phase protocol we use to determine the sign of the piezoelectric effect. Let's take the upper panel of fig. S3A as an example. In this branch, the polarization of the PZT has been switched upwards by the slow triangular waveform (positive bias in the hysteresis loop). It should be noted that the slow dc bias is applied to the bottom electrode with top electrode grounded. As a result, the "positive" field is pointing upwards from bottom electrode towards top electrode. However, in dynamic piezoelectric measurements, an additional small ac sinusoidal voltage is applied to the conductive tip in contact with the top electrode, which drives the capacitor to oscillate. In this setup, the positive branch of the ac voltage produces an electric field pointing downwards, against the polarization direction. Due to the positive d_{33} of PZT, the displacement will be negative. Once the ac voltage goes into the negative branch, the displacement will become positive. Hence, the voltage (the black sinusoidal wave) and the displacement (the green sinusoidal wave) signals are always out of phase with each other, resulting in a 180° phase lag with respect to the reference. When the polarization is switched downwards, the voltage and displacement signals are in phase, which is 0° phase lag, as shown in the lower panel of fig. S3A. Of course, if the piezoelectric effect is negative, the voltage – displacement relationship will completely opposite, as illustrated in fig. S3B. Therefore, if we know the polarization direction and the corresponding phase of the piezoelectric response, we can determine the sign of the piezoelectric effect. The polarization direction can be predetermined by applying a dc switching bias with known polarity.

Figure S4 shows the frequency-dependent dynamic piezoelectric responses. All three samples show weak frequency dispersions, confirming that the measured signals are from the intrinsic

lattice vibrations. 180° phase difference is observed for CIPS sample with upward and downward polarization, consistent with the mechanism described in fig. S3. The amplitude signals start to show anomalies when the frequency is approaching the first harmonic of the tip-sample contact resonance at around 1 MHz due to the change in vibration modes of the cantilever(*58*). Therefore, a low frequency far from the resonance (10 kHz) was chosen for the dynamic piezoelectric measurements.

To compare the results obtained using the static and the dynamic methods, effective d_{33} is obtained by linearly fitting the S – E curves around the zero field according to the equation

$$d_{33} = \left(\frac{\partial S_3}{\partial E_3}\right)^T \tag{S1}$$

The obtained values shown in fig. S5 are generally consistent with the dynamic measurements, but a bit higher, which can be considered as the static limit of the piezoelectric coefficient. To confirm the linearity of the piezoelectric response, ac voltage with different amplitudes are applied to CIPS at 10 kHz. The recorded piezoelectric amplitude is fitted linearly to produce an effective d_{33} of around -95 pm/V.

Figure S6 shows the topographic and corresponding PFM images of three samples obtained by dynamic piezoresponse methods. To check the relationship between phase contrast and polarization direction, a dc bias is applied to the AFM tip to create box-in-box patterns with opposite polarization directions, which are determined by the polarity of the bias. Consistent with the protocol described in fig. S3, oppositely polarized domains show 180° phase difference,

and the corresponding phase contrast completely reverses between PVDF, CIPS with negative piezoelectricity and PZT with positive piezoelectricity.

Section S3. Intrinsic piezoelectric response of CIPS by in situ micro-XRD

Cantilever-based displacement measurements may suffer from extrinsic effects, such as substrate deformation, the change in the cantilever vibration mode and electrostatic contribution. To reveal the intrinsic lattice contribution to the piezoelectricity, micro X-ray diffraction was employed in-situ under electric field. As shown in fig. S7 (A and B), when an electric field parallel to the existing polarization is applied, the (008) Bragg peak of CIPS single crystal moves to higher 2θ angle, suggesting the contraction of the out-of-plane lattice parameter. This observation is consistent with the negative longitudinal piezoelectric effect. The effective d_{33} can be derived based on Eq. (S1) to be -91.6 pm/V under 40 V bias. This value is very close to those acquired by static and dynamic cantilever-based techniques, confirming the results. Subsequent higher bias results in no larger or even smaller lattice deformation. We attribute this behavior to Joule heating that partially compensates the lattice contraction and also the degradation of the sample due to prolonged biasing (~ 2 mins for each scan). After 60 V bias, the sample breaks down.

In a second test, we gradually increased the voltage bias and measured the (008) peak simultaneously (fig. S7, C and D). The deduced lattice strain changes almost linearly with the applied electric field. From the linear fit, we obtained the d_{33} to be around -106 ± 10 pm/V, again, consistent with other measurement results.

Section S4. Quantitative determination of the electrostriction coefficient Q_{33}

The nature of piezoelectric effect is spontaneous polarization biased electrostriction. The static and dynamic measurements of the piezoelectric effect thus allow us to assess the electrostriction coefficient Q_{33} of three samples in two ways. The first method is based on the strain – polarization relationship through the equation

$$S_{33} = Q_{33}P_3^2 \tag{S2}$$

where S_{33} is the total longitudinal strain developed from the centrosymmetric phase and P_3 is the total electric displacement, including the spontaneous polarization P_s and the induced one P_i. Accurate determination of Q_{33} thus requires the total polarization to be precisely measured. However, typical polarization measurement using Sawyer-Tower circuit is convoluted by parasitic contributions from non-remnant polarization switching and leakage currents. To obtain the true polarization value including only P_s and P_i, the P – E loops are first fitted using the method developed by Miller and coworkers(*59*), based on the following equations

$$P_s^+(E) = P_{max}\tanh\left(\frac{E-E_c}{2\delta}\right) \tag{S3}$$

$$\delta = E_c\left[\log\left(\frac{1+\frac{P_r}{P_{max}}}{1-\frac{P_r}{P_{max}}}\right)\right]^{-1} \tag{S4}$$

where $P_s^+(E)$ is the polarization hysteresis branch with electric field ramping from negative to positive, P_{max} is the maximum polarization, P_r is the remnant polarization and E_c is the coercive

field. Similarly, the other branch with electric field ramping from positive to negative can be fitted by

$$P_s^-(E) = P_{max}\tanh(\frac{E+E_c}{2\delta}). \quad \text{(S5)}$$

The total polarization including the induced polarization can be written as

$$P_3 = P_s + \varepsilon_0\varepsilon_r E\acute{p} \quad \text{(S6)}$$

where ε_0 and ε_r are vacuum and relative permittivity, $\acute{p}$ is a parity function that takes different signs depending on the relative orientation of electric field and spontaneous polarization. The fitted polarization hysteresis loops are shown as solid lines in fig. S8. As mentioned previously, the additional contribution to polarization in CIPS is mainly leakage current due to its high ionic conductivity. After subtracting this term, the hysteresis loop becomes highly square, consistent with the single crystal nature and pure 180° polarization reversal. In comparison, PVDF and PZT samples display small leakage contributions, but certain degree of non-remnant polarization switching, probably due to additional polarization rotation. This behavior is consistent with the polycrystalline nature of the PVDF and the morphotropic phase boundaries in PZT.

Q_{33} can then be calculated according to the slope of the linear fit of the S – P^2 curves. As expected, negative Q_{33} values are obtained for PVDF and CIPS, and PZT has a positive value. It is worth pointing out that the linear fit is only valid for high polarization region, particularly the saturated polarization region shown in the P – E curves. When the polarization switching takes

place, the S – P^2 curves start to deviate from the linear relationship. This behavior is common for all three samples, and also reported for other ferroelectrics(*30*). Therefore, the hysteresis in the S – P or S – P^2 curves are due to the hysteretic polarization switching rather than the additional electromechanical coupling term as reported for PVDF(*16*). The fundamental reason can be understood from the linear fits. If we extrapolate the linear fit to P equals to zero, we should obtain the spontaneous strain. Unfortunately, this spontaneous strain is not accessible in typical strain measurements. First, "intrinsic" switching is absent for almost all ferroelectrics, in which the polarization switching is always accompanied by domain growth(*60*). Hence, the macroscopic zero polarization state is achieved by half upward and half downward polarization, rather than a true centrosymmetric state with zero strain. Even that you can probe a tiny domain region that switches as a whole, the switching time will be sub-nanoseconds(*61*), which is beyond the acquisition speed for conventional strain measurements. Therefore, the polarization-switching region of the S – P^2 curve does not follow Eq. (S2), but is determined by the probing area, domain switching dynamics as well as the data acquisition time.

The second method used to determine the Q_{33} is based on the dynamic piezoelectric measurements. As piezoelectricity in ferroelectric materials is spontaneous polarization bias electrostriction, d_{33} is the coefficient of the first-order term in the expansion of Eq. (S2) as follows

$$d_{33} = 2Q_{33}\varepsilon_0\varepsilon_r P_s. \quad \text{(S7)}$$

Hence, by measuring field-dependent d_{33} and ε_r and assuming a constant spontaneous polarization, we are able to calculate the field-dependent Q_{33}. The results are shown in fig. S9. It can be seen that field-dependent Q_{33} also shows hysteretic behavior, which is simply the result of domain switching. Once the polarization switching is completed, CIPS shows almost constant Q_{33} without field dependence. This suggests that the decrease of d_{33} at high field is purely due to the decrease of the dielectric permittivity. In comparison, Q_{33} of PVDF and PZT increase with the electric field. We believe this is an extrinsic effect due to the additional polarization rotation as seen in the P – E hysteresis loops, which makes the calculated Q_{33} larger. Nevertheless, if we look at the zero field Q_{33}, the two methods reach good agreement with previous reports(*14*, *62*), indicating the validity of both the static and dynamic piezoelectric measurements.

The spontaneous strain can be accessed in another way, using lattice anomaly around ferroelectric-paraelectric phase transition. Typical oxide/3D ferroelectrics ($PbTiO_3$ and $BaTiO_3$) show concurrent structural changes at the first-order ferroelectric (FE) – paraelectric (PE) phase transitions. When the sample is cooling down from PE phase to FE phase, a spontaneous strain will develop. From the phenomenological theory, the spontaneous strain along the polar axis $S_s = Q_{33}P_s^2$. Because in oxide/3D ferroelectrics, Q_{33} is positive, the longitudinal spontaneous strain is also positive, resulting in elongation of the lattice along *c* axis (polar axis) and concomitant shrinkage of in-plane *a* and *b* axis due to a positive Poisson's ratio (fig. S10, A and B)(*32*, *33*). The process is reversible, if the sample is heated up across the Curie temperature (Tc), the *c* lattice constant will decrease and *a* and *b* axes will increase. The temperature-dependent lattice evolution along the polar axis is thus against the thermal expansion, and leads to the anomalous negative thermal expansion at the FE-PE phase transitions(*63*).

CIPS, in contrast, shows a very different behavior in the temperature-dependent lattice evolution. Both of the out-of-plane (polar axis) and in-plane lattice parameters expand when the sample is heated across the Tc (fig. S10C)(*31*). The elongation of the *c* lattice constant of CIPS is consistent with its negative Q_{33}, which, in turn, results in its negative d_{33}. Its in-plane lattice constants, however, also increase, signifying abnormal elastic behavior in this highly anisotropic solid. According to our theoretical calculations, the Poisson's ratio v_{zx} is close to zero, which means that the in-plane and out-of-plane elastic deformations are almost independent. Lastly, it is found that the intralayer thickness and interlayer vdW gap both expand when passing through the FE-PE phase transition. This possibly suggests that both of them contribute to the negative d_{33} in CIPS.

Section S5. The "dimensional model" and Maxwell strain

The "dimensional model" is widely used to explain the negative longitudinal piezoelectric effect in ferroelectric polymers(*13*). The model assumes rigid dipole moments imbedded in an amorphous matrix. When an electric field is applied in the same direction of the existing dipoles, the surface polarization P will increase. Because P equals to M/V, where M is the total dipole moment and V is the volume of the sample, and M remains constant, the sample volume will reduce. This is achieved by the deformation of the amorphous component, since the crystalline part holds a fixed dipole moment. Mathematically, the effective d_{33} due to the dimensional effect can be described as

$$d_{33} = -\frac{P_r}{C_{33}} \tag{S12}$$

where P_r is the remanent polarization and C_{33} is the longitudinal elastic modulus. Taking a value of 8 μC/cm^2 for P_r and 3.1 GPa for $C_{33(64)}$, the calculated d_{33} is around -26 pm/V, very close to the commonly reported values for PVDF(*14*). CIPS possesses a similar dipole structure as PVDF with isolated sheets: the atomic layers are assumed to hold rigid dipole moments and the vdW gap can be deemed as compliant space (fig. S11). We then try to use this model to estimate the magnitude of negative d_{33}. Taking a value of 4 μC/cm^2 for P_r and 25 GPa for C_{33} (see Supplementary Text 6), the calculated d_{33} for CIPS is -1.5 pm/V, which is negligible compared to the measured value of ~-95 pm/V. Besides, the "dimensional model" provides only a vague phenomenological description of the negative longitudinal piezoelectric effect. It doesn't clarify the microscopic drive for the compression of the amorphous part. Apparently, this model cannot explain the giant negative d_{33} of CIPS.

Maxwell strain is another mechanism often adopted to describe the negative electrostriction effect in polymers and soft materials(*38*). Basically it describes that the electrostatic attractive force between two oppositely charged electrodes will compress the sample, and that is why the electrostriction is always negative. The attractive force between the two metal plates of a capacitor can be found in common physics textbooks and is expressed as

$$F = \frac{1}{2}\varepsilon_0 A E^2 \tag{S13}$$

where ε_0 is the vacuum permittivity, A is the area of the capacitor and E is the electric field. When the vacuum is replaced by a dielectric, a common belief is that the force will become

$$F = \frac{1}{2}\varepsilon A E^2 \tag{S14}$$

where ε is the absolute permittivity of the dielectric(*30*). Hence, the longitudinal Maxwell strain for dielectrics can be expressed as

$$S_M = \frac{F}{AC_{33}} = -\frac{1}{2}\frac{\varepsilon E^2}{C_{33}} \tag{S15}$$

where C_{33} is the elastic modulus. This doesn't apply to materials with continuous lattice, because the internal dipole charges cancel out, leaving only bound charges that are largely screened by the metal electrodes. However, it holds for materials with reduced lattice dimensionality, in which dipoles are isolated, and the intermolecular space with weak interactions that account for the materials' elastic constant can be compressed by the Maxwell stress. Similar to normal electrostriction, Maxwell strain also varies quadratically with electric field, and the apparent electrostrictive coefficient Q_{33} is determined by

$$\frac{S_M}{P^2} = \frac{S_M}{(\varepsilon E)^2} = -\frac{1}{2\varepsilon C_{33}} \tag{S16}$$

In soft materials, due to the small C_{33}, the Maxwell strain can be very large. Based on Eq. S16, we can estimate the electrostriction coefficient of CIPS to be -0.07 m^4C^{-2}, way off compared to experimental value of -3.4 m^4C^{-2}. Apparently, the Maxwell strain alone cannot explain the giant negative electrostriction in CIPS.

In ferroelectrics, if we adopt the phenomenological description of d_{33} as $2Q_{33}\varepsilon P_r$, we obtain the apparent $d_{33} = -2\frac{1}{2\varepsilon C_{33}}\varepsilon P_r = -\frac{P_r}{C_{33}}$, which has the same mathematical expression as that of the "dimensional model". This is because the "dimensional model" and Maxwell strain are of the same physical origin, namely, the electrostatic attraction with increasing dipole moment. Our rigid ion model shown in Fig. 3D is in accordance with the "dimensional model" and Maxwell strain at a microscopic scale. The 2D layered structure of CIPS can be viewed as a series of parallel capacitors separated by vdW gap. When the applied field increases the surface charge density of the system, according to Gauss's law, the field across the vdW gap would be much larger than that across the layer due to much lower polarizability. Besides, the C_{33} of the vdW gap is much smaller than that of the layer. As a result, the microscopic Maxwell strain across the vdW gap will become dominant based on Eq. S16, which explains the giant electrostriction coefficient leading to negative longitudinal piezoelectricity/electrostriction, provided this effect is dominant over other adverse effect, such as that shows in conventional ferroelectrics (Fig. 3E). This is the case for materials with reduced lattice dimensionality, where the weak intermolecular interactions are much more susceptible to electrostatic energy change.

Section S6. Thickness-dependent piezoelectric response, clamping effect, and electromechanical coupling factor

The CIPS samples disucssed in the maintext are thin crystals with thickness around 5 – 15 μm, whereas the thicknesses of PVDF and PZT samples are in the range of 100 – 200 nm. To check if there is any thickness dependence, thin CIPS flakes are mechanically exfoliated on highly-doped Si substrates. Au top electrodes with the lateral sizes of 4 -100 μm^2 are then fabricated. The piezoelectric responses of the capacitors are measured using the dynamic method, and the results are summarized in fig. S16. It is observed that the phase hysteresis loops show the same trend for CIPS flakes with different thicknesses, confirming the negative piezoelectric effect. Besides, we observe weak decline of the piezoelectric response when the thickness is reduced from 6 μm to 100 nm. This can be attributed to the weak clamping effect in 2D vdW ferroelectrics. Similarly, for the 1D PVDF, the effective d_{33} we obtained for a 130-nm-thick film is around 25 – 30 pm/V, comparable to micrometer-thick bulk samples(*14*). In contrast, 3D ferroelectrics such as PZT show significant clamping effect with reduced thickness(*64, 65*). For ferroelectric thin film under full clamping, the in-plane strain induced by the electric field equals to zero. Following Lefki and Dormans, the measured d_{33} can be expressed by the equation(*66*)

$$d_{33}^{measured} = d_{33} - \frac{2d_{31}s_{13}^{E}}{s_{11}^{E}+s_{12}^{E}} \quad \text{(S8)}$$

where d_{33} and d_{31} are the intrinsic longitudinal and transverse piezoelectric coefficients of the bulk material, respectively; s_{ij}^{E} are the elastic compliances of the film under constant electric field. Since $d_{31,}$ s_{12} and s_{13} are usually negative, and s_{11} is positive but larger than s_{12}. The measured d_{33} is usually suppressed in thin film than that of the bulk, as can be seen in the PZT

case. However, for low-dimensional ferroelectrics, if the polar axis is along the crystallographic direction with weak intermolecular bond and perpendicular to that with strong intramolecular bond, the poisson's ratio is expected to be small(*67*). As a result, the transverse piezoelectric coefficient d_{31} will be negligible. Consequently, the suppression of d_{33} due to the substrate clamping (second term of Eq. (S8)) is small. This unique quality makes low-dimensional vdW ferroelectrics/piezoelectrics highly promising for flexible nanoelectromechanical applications compared to the 3D counterparts(*68, 69*). This explains why CIPS outperforms PZT with MPB composition in the comparable thickness range (100 – 300 nm).

Another important figure of merit for piezoelectric materials is the electromechanical coupling factor *k*, defined as the effectiveness of conversion between electrical energy and mechanical energy. Specifically, the quasistatic thickness-extensional coupling factor of thin plates k_{33}^{t} can be calculated by

$$k_{33}^{t} = d_{33}\sqrt{\frac{C_{33}}{\varepsilon_{33}}} \tag{S9}$$

where C_{33} is the elastic or Young's modulus (reciprocal of s_{33}) and ε_{33} is the dielectric permittivity(*70*). The d_{33} and ε_{33} values of PVDF, CIPS and PZT samples were measured experimentally. The out-of-plane elastic moduli of PVDF and PZT have been widely reported in literature, which show large variations in numbers, depending on the fabrication method, sample crystallinity/orientation and measurement technique. For PVDF, it ranges from 1 to 3 GPa(*13, 14, 71*), while for PZT, it is around 100 – 150 GPa(*26, 72–74*). There is no report on the mechanical properties of CIPS. To determine its Young's modulus, we performed nanoindentation test on 10

– 30 μm-thick single crystals using a commercial nanoindenter (NanoTest, Micromaterials Ltd). Special care was taken to ensure solid contact between the sample stack and the single crystals. The indentation depth was kept well below 1/10 of the total thickness of the single crystal. Typical indentation results are shown in fig. S17. The reduced modulus can then be deduced from the slope of load – displacement curve, dP/dh, upon unloading, using Oliver and Pharr's method(*75*)

$$C_r = \frac{dP}{dh}\frac{1}{2\beta}\frac{\sqrt{\pi}}{\sqrt{A}} \tag{S10}$$

where C_r is the reduced Young's modulus, β is the geometry constant close to unity (1.034 for Berkovich indenter), and A is the projected area of the indentation at the contact depth h_c. For a Berkovich tip, $A \cong 24.5\, h_c^2$. The reduced modulus C_r is related to Young's modulus C_{33} through the following relationship from contact mechanics

$$\frac{1}{C_r} = \frac{1-\nu^2}{C_{33}} + \frac{1-\nu_i^2}{C_i} \tag{S11}$$

where C_i is the elastic modulus of the indenter (1140 GPa for diamond), ν and ν_i are the Poisson's ratios of the sample and the indenter. The Poisson's ratio of diamond is 0.07 and that of CIPS is likely close to zero. The C_{33} of CIPS is calculated to be around 25 ± 5 GPa.

Using Eq. (S9), we can then calculate the electromechanical coupling factor for all three samples, and the results are summarized in Table 1 in the maintext. The obtained values for PVDF is around 0.1-0.16, and for PZT is around 0.41-0.5, in reasonable agreement with the literature, but

slightly smaller than those with best performance reported(*76, 77*). Surprisingly, CIPS shows a high electromechanical coupling factor comparable to the best-performing piezoelectric materials(*78*), which makes it very suitable for sensors and transducers.

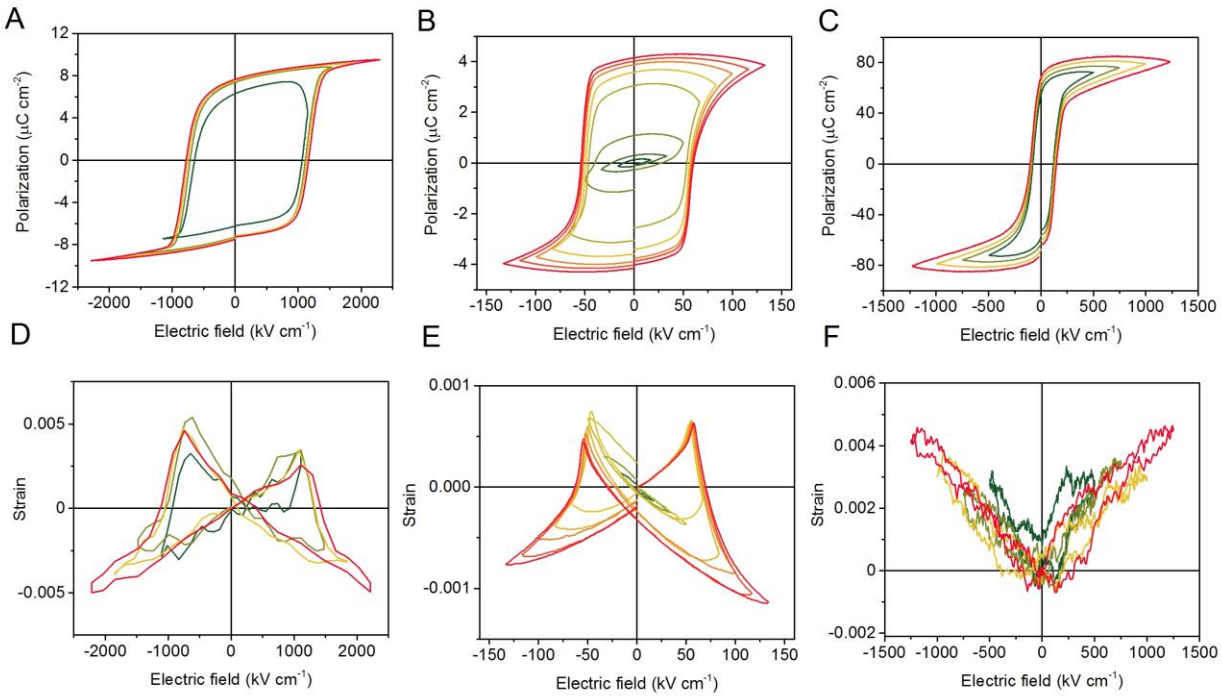

Fig. S1. Voltage-dependent P-E and S-E hysteresis curves. (**A-C**) Voltage dependent P – E loops of PVDF at 1 kHz (A), CIPS at 100 Hz (B), and PZT at 100 Hz (C). (**D-F**) Concurrently recorded S – E loops of PVDF at 1 kHz (D), CIPS at 100 Hz (E), and PZT at 100 Hz (F).

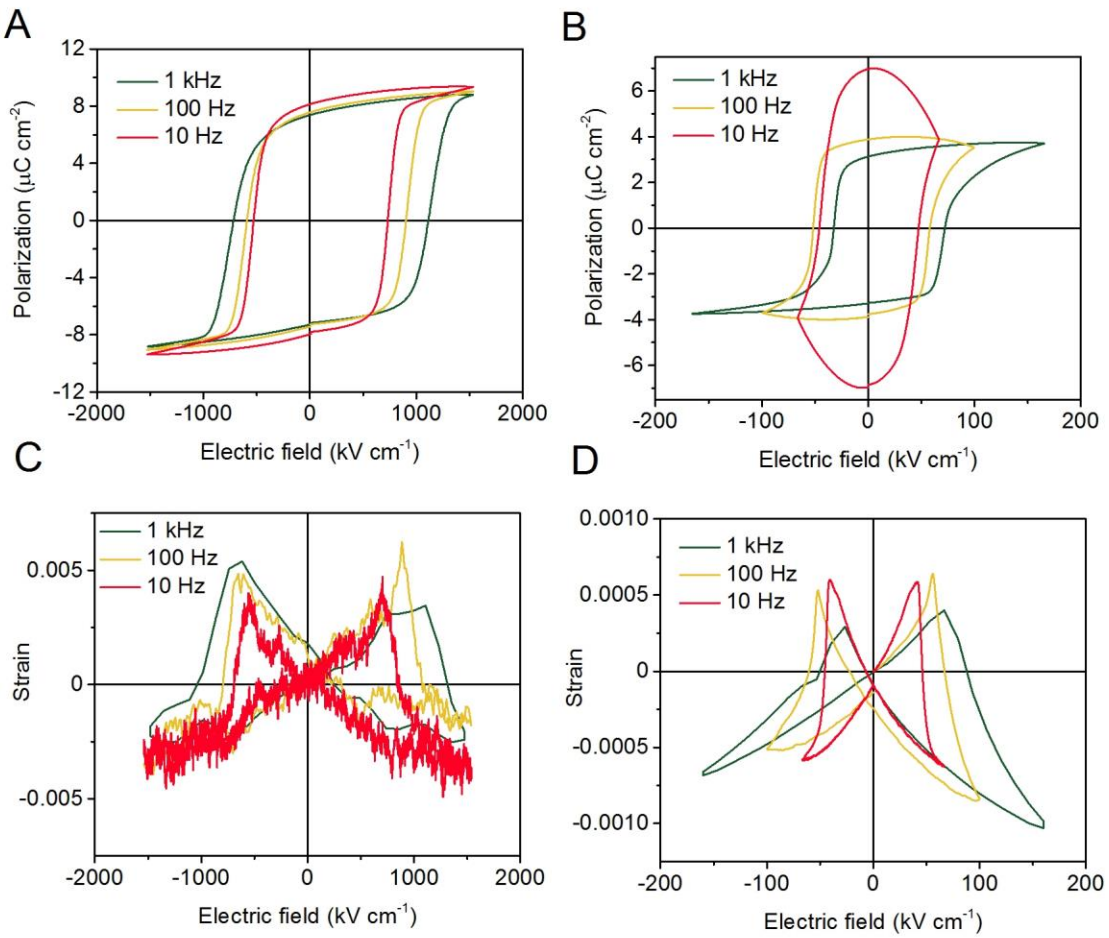

Fig. S2. Frequency-dependent P-E and S-E hysteresis curves. (**A** and **B**) Frequency dependent P – E loops of PVDF (A) and CIPS (B). (**C** and **D**) Frequency dependent S – E loops of PVDF (C) and CIPS (D).

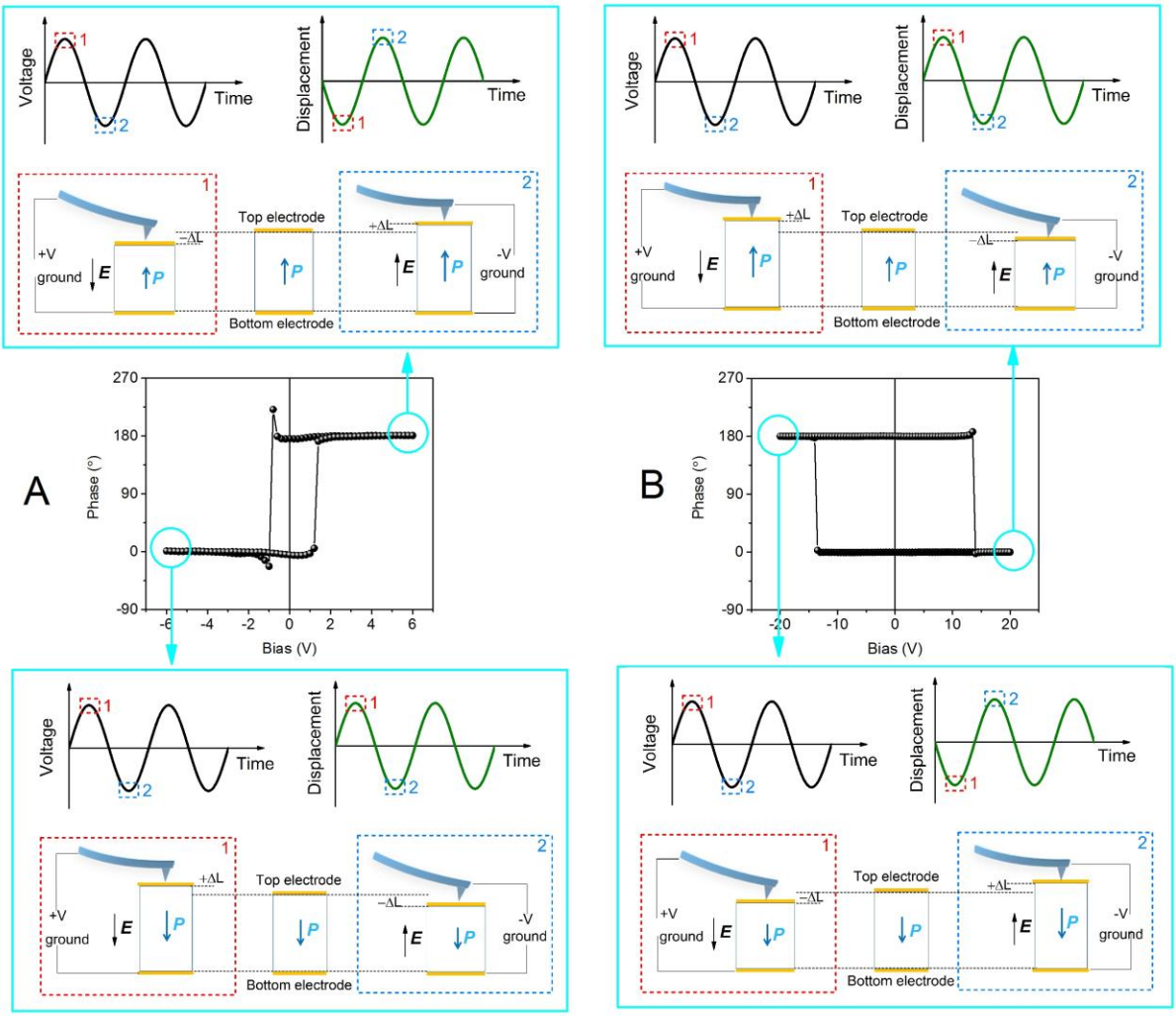

Fig. S3. Voltage-displacement phase relationship in dynamic piezoelectric measurements. (**A**) The situation of positive piezoelectric effect. Upper panel: when the polarization is pointing upwards, the voltage and displacement signals are out of phase, corresponding to a 180° phase lag. Middle panel: Representative phase hysteresis loop of PZT. Lower panel: when the polarization is pointing downwards, the voltage and displacement signals are in phase, corresponding to a 0° phase lag. (**B**) The situation of negative piezoelectric effect. Upper panel: when the polarization is pointing upwards, the voltage and displacement signals are in phase, corresponding to a 0° phase lag. Middle panel: Representative phase hysteresis loop of CIPS.

Lower panel: when the polarization is pointing downwards, the voltage and displacement signals are out of phase, corresponding to a 180° phase lag.

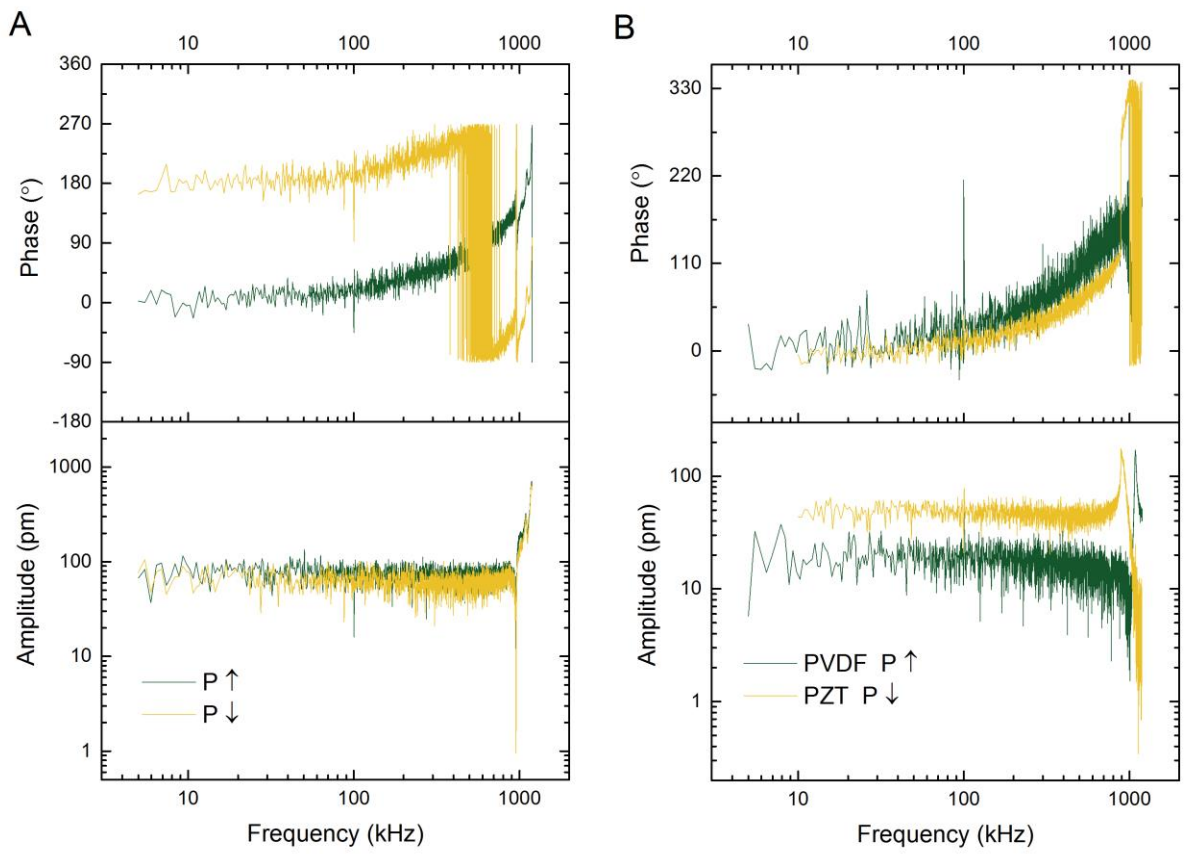

Fig. S4. Frequency-dependent piezoelectric response. (**A**) Frequency dependent amplitude and phase signals of CIPS for upward and downward polarization states. (**B**) Frequency dependent amplitude and phase signals of PZT with downward polarization and PVDF with upward polarization. The anomalies at 100 kHz is due to a system noise.

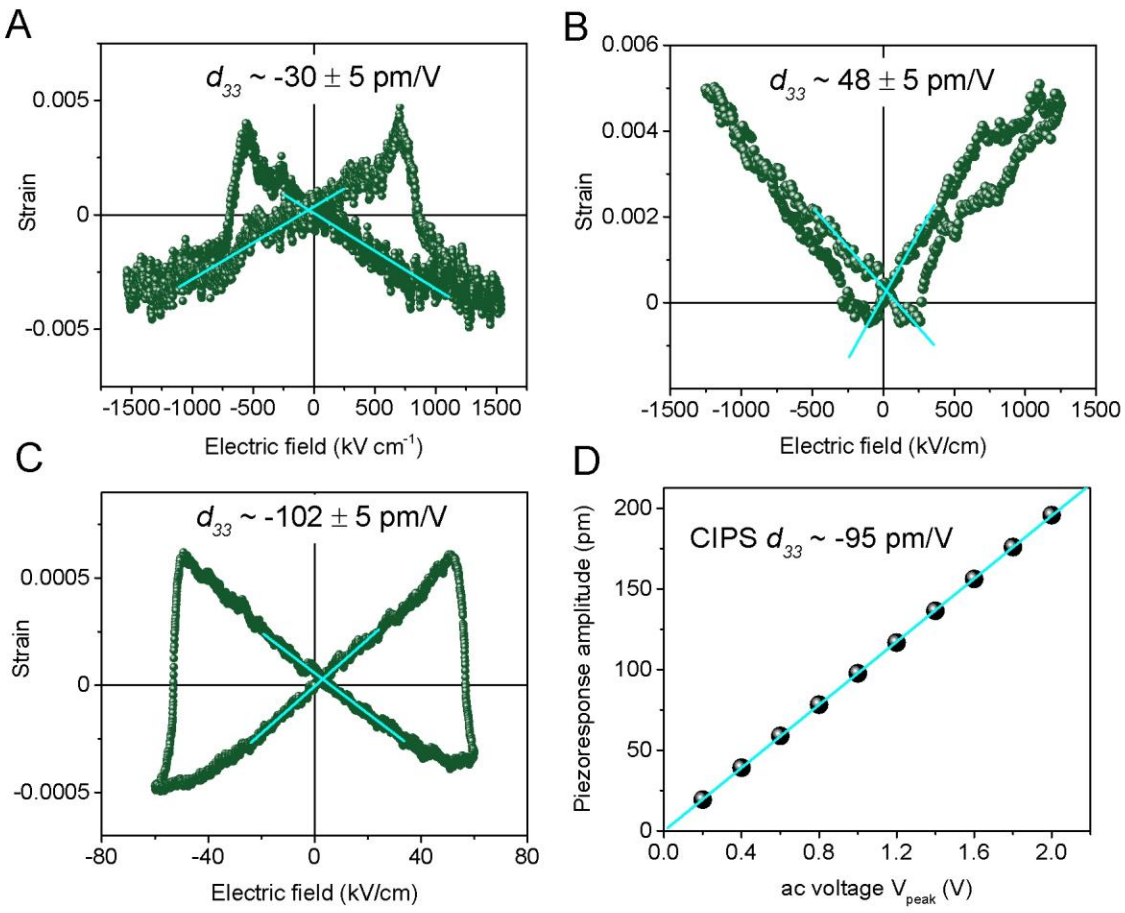

Fig. S5. Determining the static d_{33} from S-E curves. (**A-C**) Static d_{33} of PVDF (A), PZT (B), and CIPS (C) obtained by fitting the slope of S – E curve around the zero field. The obtained values agree well with those from dynamic measurements. (**D**) Ac voltage dependent piezoresponse of CIPS in dynamic piezoelectric measurement. The linear relationship confirms the measured signal originates from the linear piezoelectric effect.

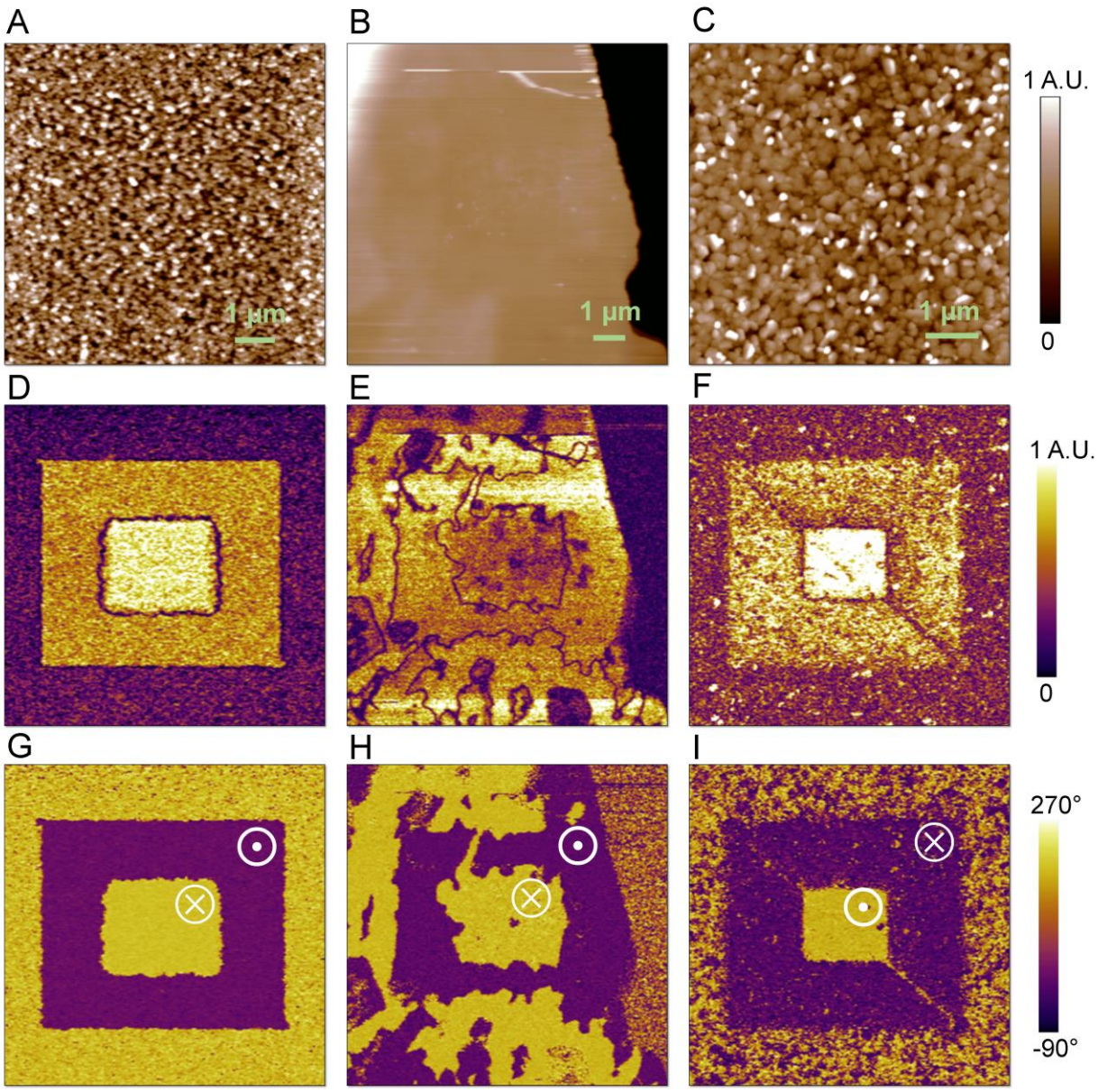

Fig. S6. PFM images with box-in-box patterns written. (**A-C**) Topographic images of PVDF (A), CIPS flake (B) and PZT (C). (**D-F**) Corresponding PFM amplitude images of (D), CIPS flake(E) and PZT (F). (**G-I**) Corresponding PFM phase images of (G), CIPS flake (H) and PZT (I). The color tones of the box-in-box patterns indicate that the longitudinal piezoelectric coefficients of PVDF and CIPS are negative, whereas that of PZT is positive.

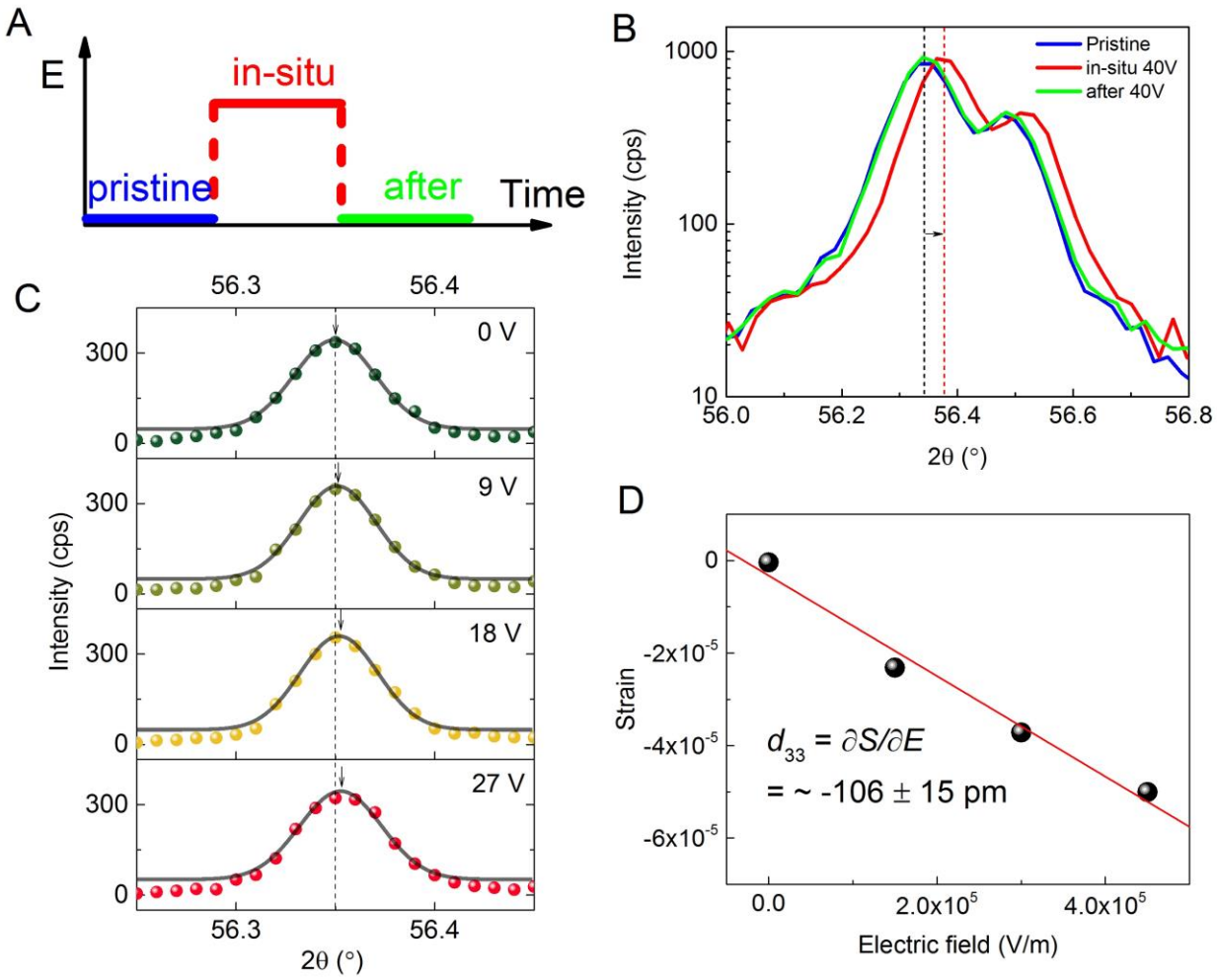

Fig. S7. In situ XRD measurements of the CIPS lattice parameter under electric field. (**A** and **B**) Electric field – time profile (A) and the corresponding XRD pattern of (008) peak of CIPS single crystal (B). (**C**) In-situ XRD patterns of the (008) peak with the stepwise increase of the applied electric field. (**D**) Strain versus electric field data from (C). The slope ($\frac{\partial S}{\partial E}$) gives the d_{33} value.

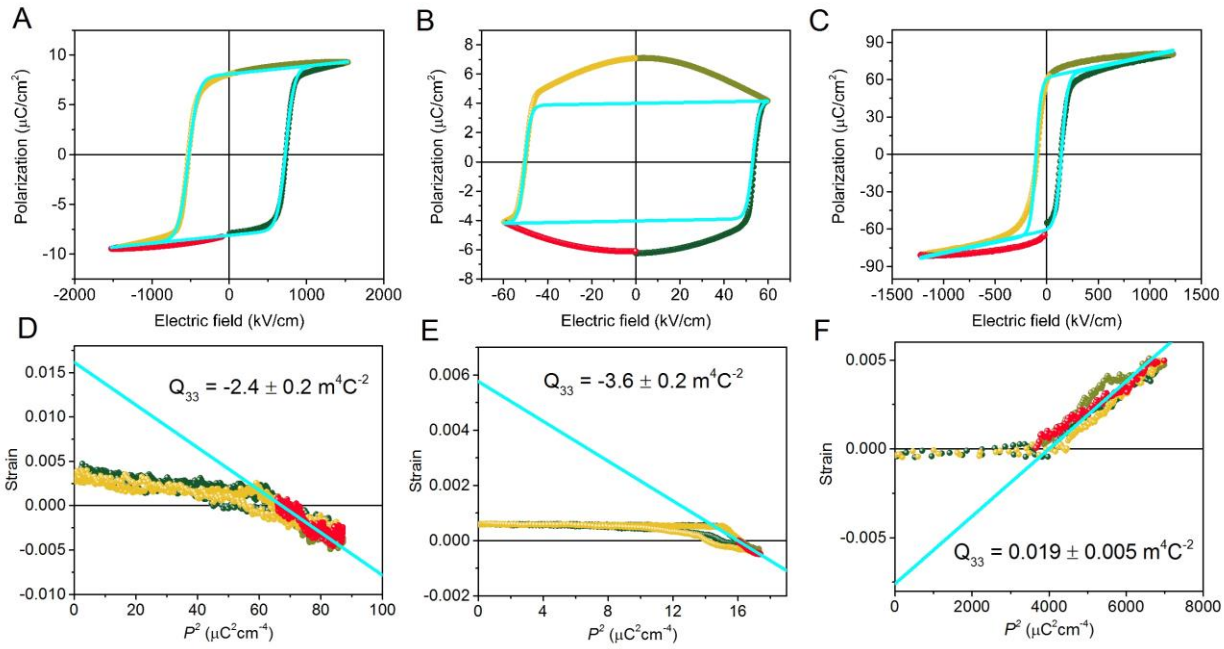

Fig. S8. Quantitative determination of electrostriction coefficient Q_{33} by linearly fitting the S-P^2 curves. (**A-C**) Modeling of ferroelectric P - E hysteresis loops of PVDF (A), CIPS (B), and PZT (C). (**D-F**) Linear fits of the strain versus P^2 curves of PVDF (D), CIPS (E), and PZT (F). The fitted curves are illustrated by the cyan solid lines.

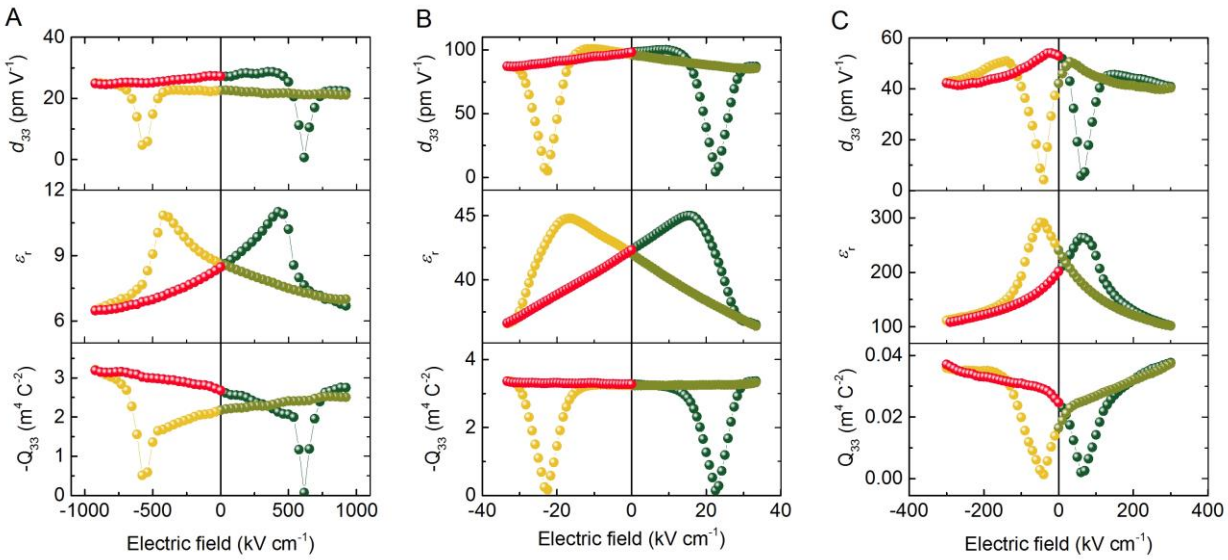

Fig. S9. Quantitative determination of electrostriction coefficient Q_{33} by $Q_{33} = d_{33}/2\varepsilon_{33}P$s. (**A-C**) Associated switching curves of piezoelectric coefficient d_{33}, relative permittivity ε_r, and calculated Q_{33} of PVDF (A), CIPS (B) and PZT (C).

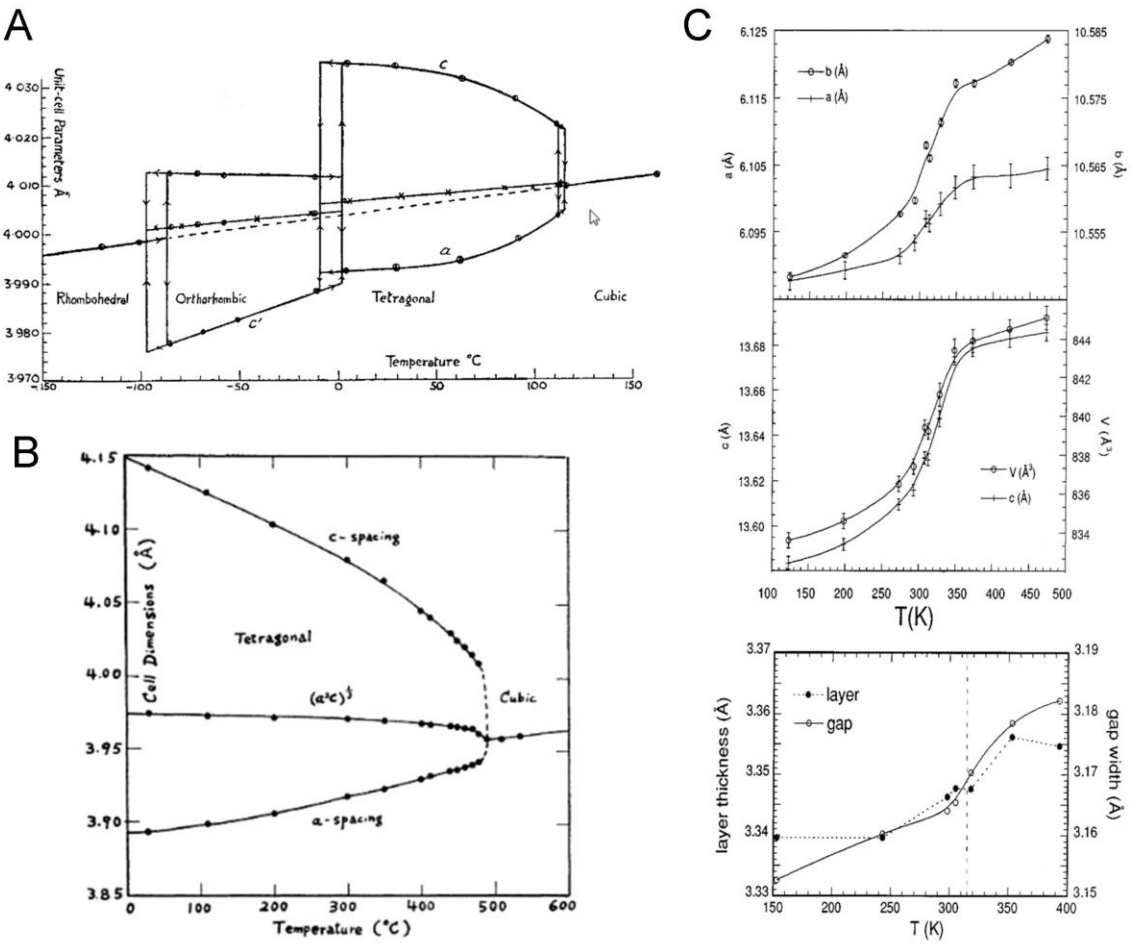

Fig. S10. Lattice anomaly around the ferroelectric-paraelectric phase transition. (**A-C**) Temperature-dependent evolutions of lattice parameters across the ferroelectric-paraelectric phase transitions of BaTiO3 (A) (Reprinted figure from (*32*) by permission of Taylor & Francis Ltd.), PbTiO3 (B) (Reprinted figure with permission from (*33*). Copyright (1950) by the American Physical Society.) and CIPS (C) (Reprinted figure with permission from (*31*). Copyright (1997) by the American Physical Society.). The changes of cell volume, intralayer thickness and vdW gap thickness of CIPS are also shown in (C).

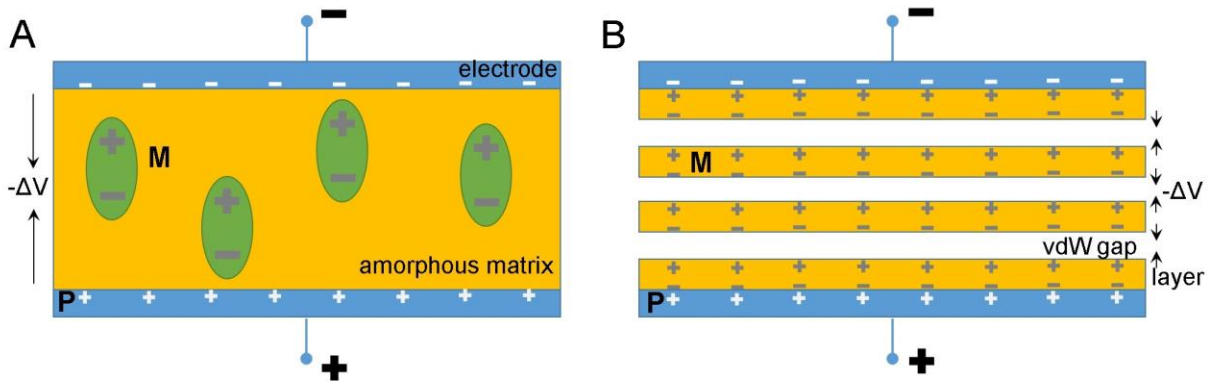

Fig. S11. Comparison between the dimensional model and reduced lattice dimensionality induced negative piezoelectricity. (**A**) The "dimensional" model widely used to explain the negative piezoelectricity in semicrystalline PVDF. (**B**) Negative piezoelectricity due to reduced lattice dimensionality in crystalline CIPS.

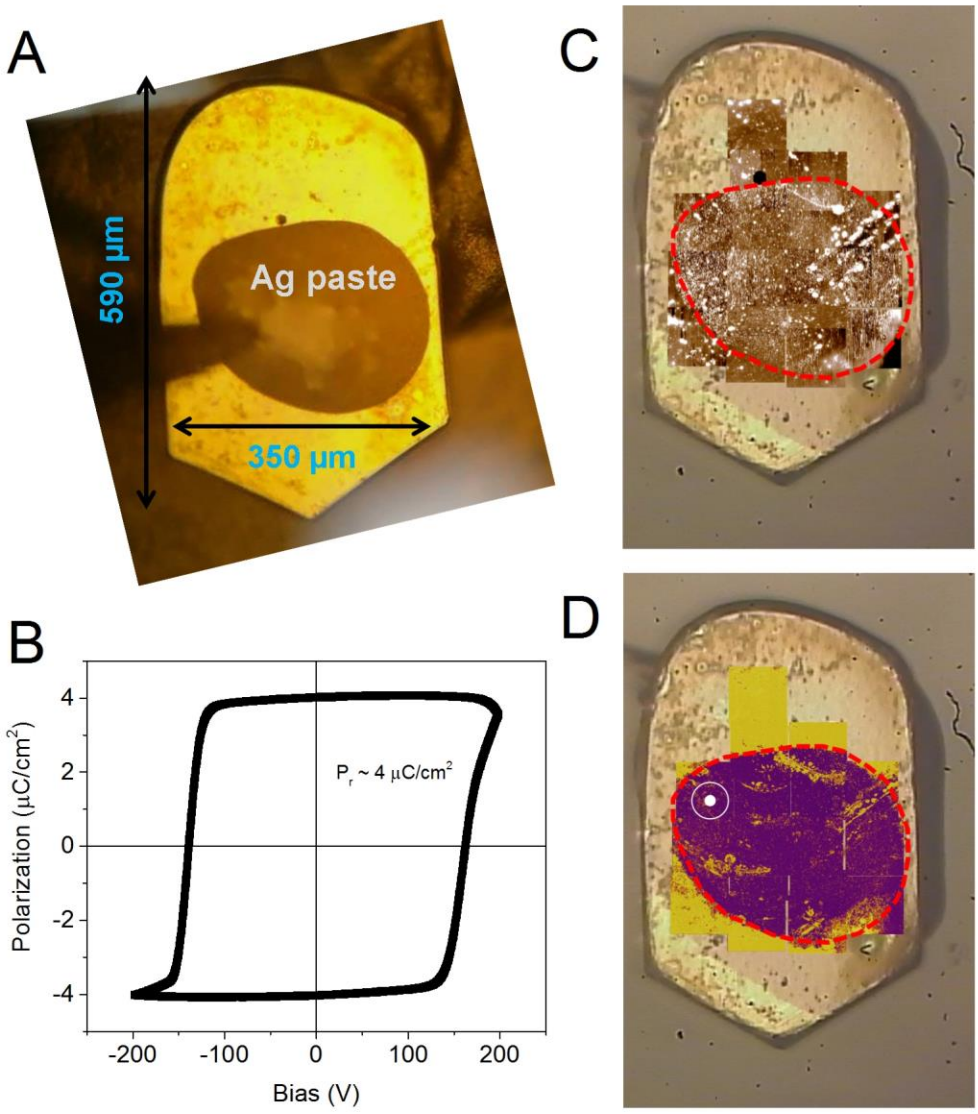

Fig. S12. Switching the polarization of CIPS for single-crystal x-ray crystallography. (**A**) Optical image of a 40-µm-thick CIPS single crystal with the Ag paste as electrode contacts. (**B**) Recorded polarization hysteresis loop during the sample poling. (**C** and **D**) Stitched 17 topographic (C) and PFM phase (D) images (80×80 µm^2) overlaid onto the optical image of CIPS crystal, showing the polarization in the central area was poled upwards. The red solid lines denote the area covered by Ag paste.

It should be noted that though the as-grown (unpoled) area shows a uniform opposite phase contrast, it doesn't mean it is in a single polarization downward state. Based on our findings from the single-crystal XRD (flack parameter close to 0.5) and the initial P – E loop measurements (need repeatedly cycling to obtain fully polarized state), it is found most of the as-grown crystals are in an unpolarized state with half polarization up and half down. The appeared downward polarization phase signal could come from electrochemical strain due to the finite ionic conductivity of CIPS. We will discuss this in more details in a separate study.

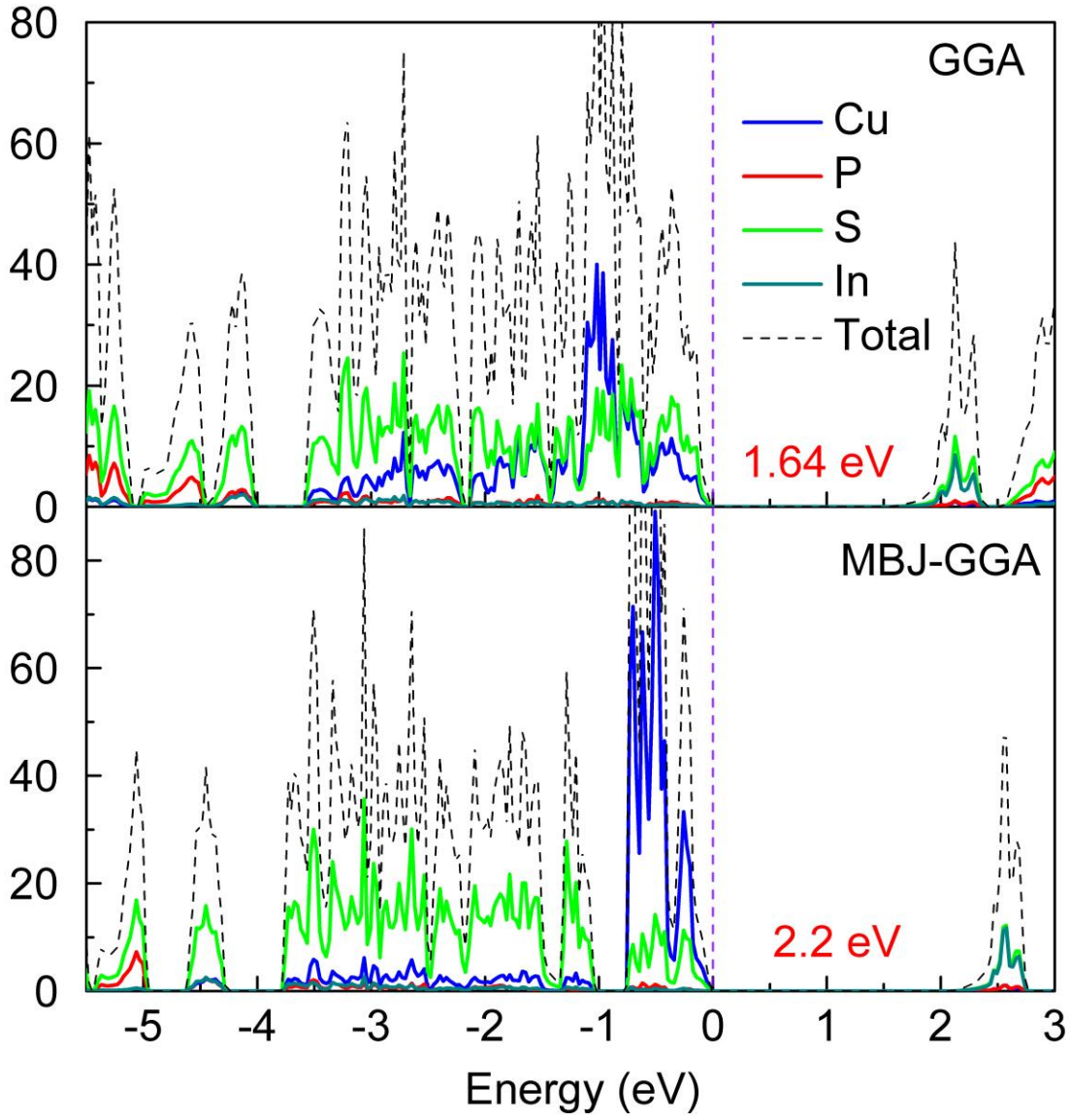

Fig. S13. Calculated DOS of CIPS.

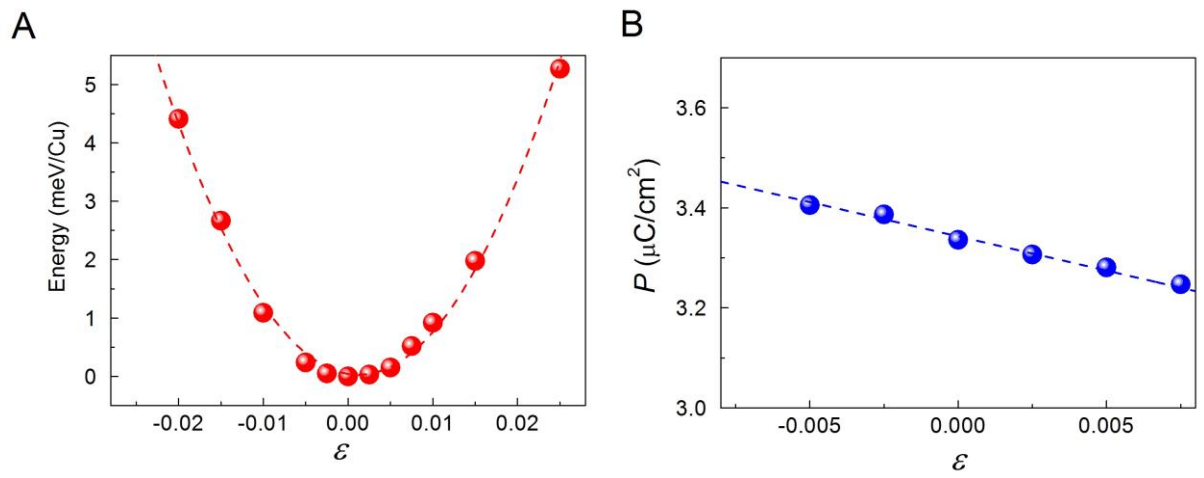

Fig. S14. Calculated energy and polarization changes as a function of applied strain. (**A**) Energy - strain curve from which the elastic modulus C_{33} can be obtained by $C_{33} = \frac{1}{V_0}\frac{\partial^2 U}{\partial^2 \varepsilon} = 7.5\ Gpa$, where V_0 is the unit cell volume at zero strain. (**B**) Polarization – strain curve. The slope of the linear fit leads to the piezoelectric coefficient $e_{33} = \frac{\partial P}{\partial \varepsilon} = -0.137\ C/m^2$. d_{33} can then be derived by $d_{33}=e_{33}/C_{33}$= -18 pC/N.

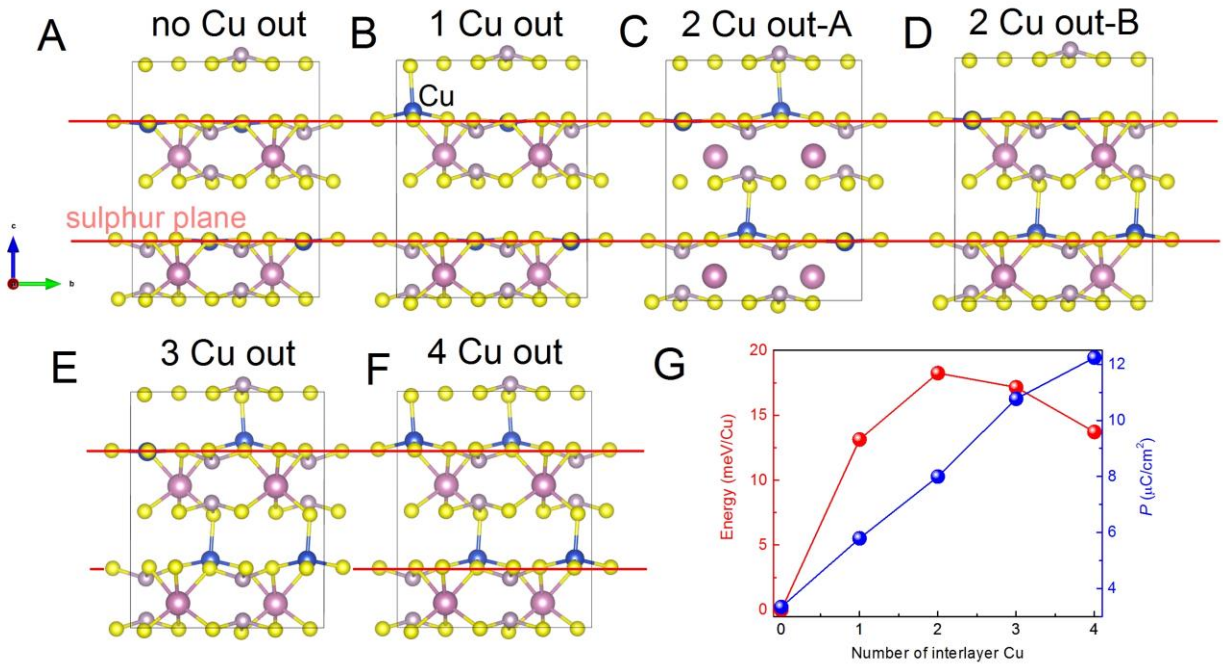

Fig. S15. Energy and polarization changes as a function of interlayer Cu ratio. (**A-F**) Atomic configurations of CIPS at ground state and with different numbers of Cu atoms at the interlayer site. (**G**) Energy and polarization changes as a function of the number of interlayer Cu atoms in the unit cell. Note that there are two possible configurations for 2-Cu-out state, so their average energy/polarization is shown.

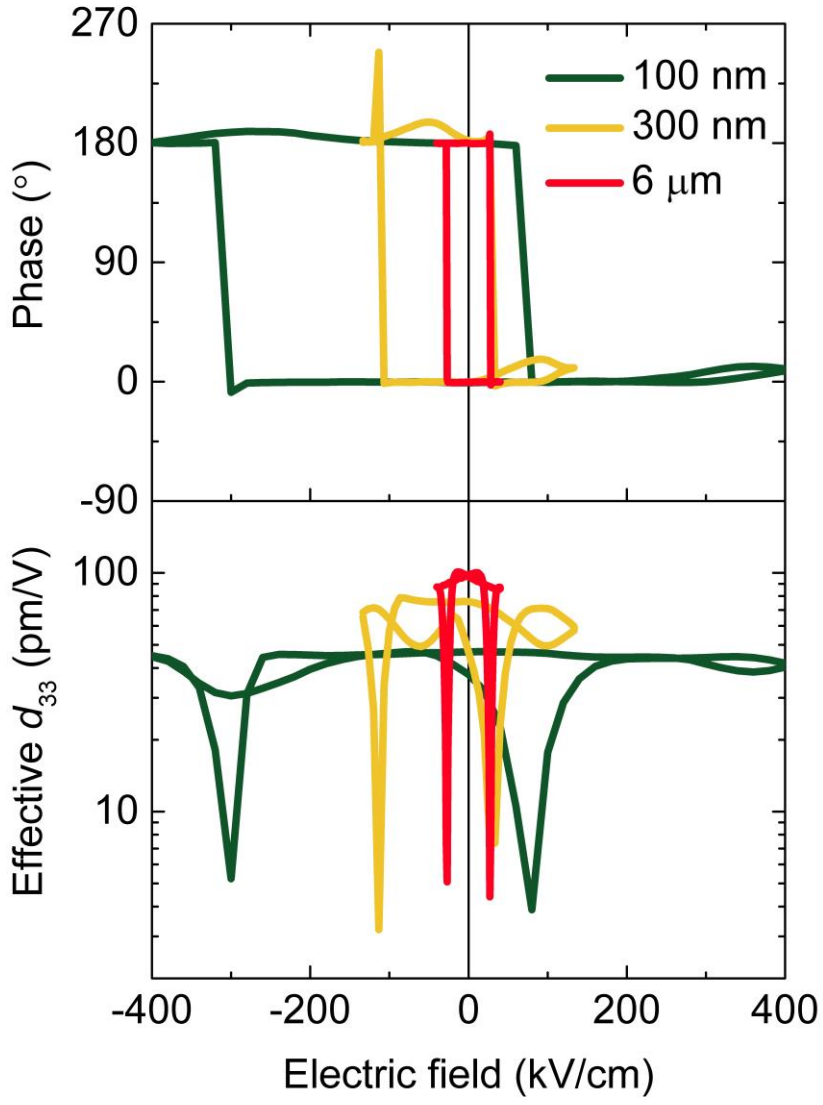

Fig. S16. Dynamic piezoelectric measurements of CIPS flakes with different thicknesses.

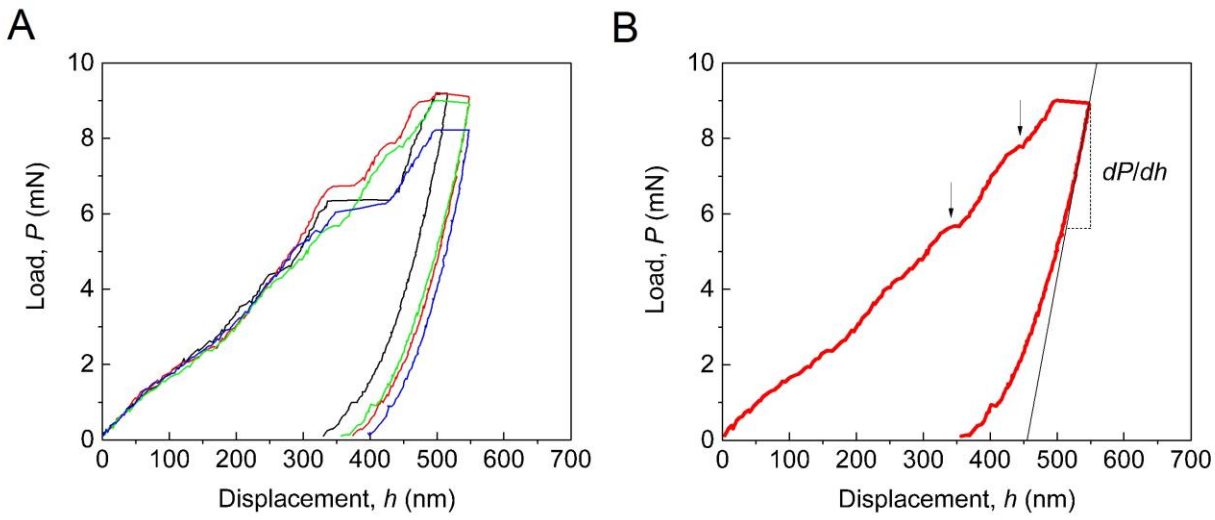

Fig. S17. Nanoindentation test of CIPS single crystal. (**A**) Load – displacement curves at random locations showing similar behavior. (**B**) Representative indentation curve used for the calculation of Young's modulus. The arrows indicate pop-ins due to fracture events.